Mon. Not. R. Astron. Soc. **000**, 000–000 (0000) Printed March 2, 2022 (MN LATEX style file v2.2)

Modelling The Redshift-Space Three-Point Correlation Function in SDSS-III

Hong Guo[1⋆], Zheng Zheng[1], Y. P. Jing[2,3], Idit Zehavi[4], Cheng Li[5], David H. Weinberg[6,7], Ramin A. Skibba[8], Robert C. Nichol[9], Graziano Rossi[10,11], Cristiano G. Sabiu[12], Donald P. Schneider[13,14], Cameron K. McBride[15]

[1] *Department of Physics and Astronomy, University of Utah, UT 84112, USA*
[2] *Center for Astronomy and Astrophysics, Department of Physics and Astronomy, Shanghai Jiao Tong University, Shanghai 200240, China*
[3] *IFSA Collaborative Innovation Center, Shanghai Jiao Tong University, Shanghai 200240, China*
[4] *Department of Astronomy, Case Western Reserve University, OH 44106, USA*
[5] *Partner Group of the Max Planck Institute for Astrophysics and Key Laboratory for Research in Galaxies and Cosmology of Chinese Academy of Sciences, Shanghai Astronomical Observatory, Nandan Road 80, Shanghai 200030, China*
[6] *Department of Astronomy, Ohio State University, Columbus, OH 43210, USA*
[7] *Center for Cosmology and Astro-Particle Physics, Ohio State University, Columbus, OH 43210, USA*
[8] *Center for Astrophysics and Space Sciences, University of California, 9500 Gilman Drive, San Diego, CA 92093, USA*
[9] *Institute of Cosmology & Gravitation, Dennis Sciama Building, University of Portsmouth, Portsmouth, PO1 3FX, UK*
[10] *Department of Astronomy and Space Science, Sejong University, Seoul, 143-747, Korea*
[11] *CEA, Centre de Saclay, Irfu/SPP, F-91191 Gif-sur-Yvette, France*
[12] *Korea Institute for Advanced Study, Dongdaemun-gu, Seoul 130-722, Korea*
[13] *Department of Astronomy and Astrophysics, The Pennsylvania State University, University Park, PA 16802*
[14] *Institute for Gravitation and the Cosmos, The Pennsylvania State University, University Park, PA 16802*
[15] *Harvard-Smithsonian Center for Astrophysics, 60 Garden St., Cambridge, MA 02138, USA*

March 2, 2022

ABSTRACT

We present the measurements of the redshift-space three-point correlation function (3PCF) for $z \sim 0.5$ luminous red galaxies of the CMASS sample in the Sloan Digital Sky Survey-III Baryon Oscillation Spectroscopic Survey Data Release 11. The 3PCF measurements are interpreted within the halo occupation distribution (HOD) framework using high-resolution N-body simulations, and the model successfully reproduces the 3PCF on scales larger than $1\,h^{-1}\mathrm{Mpc}$. As with the case for the redshift-space two-point correlation functions, we find that the redshift-space 3PCF measurements also favour the inclusion of galaxy velocity bias in the model. In particular, the central galaxy in a halo is on average in motion with respect to the core of the halo. We discuss the potential of the small-scale 3PCF to tighten the constraints on the relation between galaxies and dark matter haloes and on the phase-space distribution of galaxies.

Key words: galaxies: distances and redshifts — galaxies: haloes — galaxies: statistics — cosmology: observations — cosmology: theory — large-scale structure of Universe

1 INTRODUCTION

Contemporary galaxy redshift surveys enable the large-scale distribution of galaxies to be accurately mapped in redshift space. Compared to the real-space distribution, that in redshift space is distorted as a result of galaxy peculiar velocities, which is generally referred to as redshift space distortions (RSD). The RSD effects encode information about the kinematics of galaxies inside dark matter haloes and the growth rate of cosmic structure.

The clustering of galaxies in redshift space has been extensively studied using the two-point correlation functions (2PCFs) (Zehavi et al. 2002, 2005, 2011; Wang et al. 2004, 2007; Li et al. 2006; Coil et al. 2006; Skibba & Sheth 2009; Li et al. 2012; Guo et al. 2013). The widely-used halo occupation distribution (HOD) modelling of the galaxy 2PCFs provides an opportunity to understand the connection between galaxies and their host dark matter haloes (Jing et al. 1998; Peacock & Smith 2000; Scoccimarro et al. 2001; Berlind & Weinberg 2002; Zheng et al. 2005, 2009; Miyatake et al. 2013; Guo et al. 2014b). The observationally constrained relation between galaxies and dark matter haloes provides insight also about galaxy formation and cosmology. Recently, Guo et al. (2015) (hereafter G15) used the luminous

⋆ E-mail: hong.guo@utah.edu

red galaxies (LRGs) in the Sloan Digital Sky Survey-III (SDSS-III; Eisenstein et al. 2011) Baryon Oscillation Spectroscopic Survey (BOSS; Dawson et al. 2013) to model the redshift-space 2PCFs and found differences between galaxy and dark matter velocity distributions inside haloes, an effect denoted as galaxy velocity bias (see also Reid et al. 2014).

Higher-order statistics, e.g. the three-point correlation function (3PCF), aid in tightening the constraints on HOD parameters and in breaking the degeneracy among parameters (Kulkarni et al. 2007; Smith et al. 2008). The 3PCF, $\zeta(r_1, r_2, r_3)$, describes the probability of finding galaxy triplets with the separations in between as r_1, r_2 and r_3 (see Bernardeau et al. 2002 for a review). A non-zero 3PCF naturally arises because of the non-Gaussianity generated during the nonlinear evolution of the density fluctuations, even if primordial fluctuations were perfectly Gaussian. The 3PCF is commonly used to break the degeneracy between the galaxy bias and the amplitude of the matter density fluctuation, and therefore constrains cosmological parameters (Gaztanaga & Frieman 1994; Jing & Börner 2004; Gaztañaga et al. 2005; Zheng 2004; Pan & Szapudi 2005; Guo & Jing 2009; McBride et al. 2011; Marín et al. 2013; Guo et al. 2014c).

In this Letter, we measure the redshift-space 3PCF for the same sample of LRGs at redshift $z{\sim}0.5$ as in G15 and interpret the 3PCF measurements within the HOD framework. In particular, we perform HOD modelling of both the 2PCFs and 3PCF and investigate the additional constraining power from the 3PCF on the HOD parameters, including the galaxy velocity bias.

In Section 2, we briefly describe the galaxy sample, the 3PCF measurements, and the modelling method. We present our modelling results in Section 3 and conclude in Section 4. Throughout this Letter we adopt a spatially flat ΛCDM cosmology with a matter density parameter $\Omega_m = 0.27$, $\sigma_8 = 0.82$ and a Hubble constant $H_0 = 100h\,\mathrm{kms}^{-1}\mathrm{Mpc}^{-1}$ with $h = 0.7$.

2 DATA AND MEASUREMENTS

In this Letter, we use the same volume-limited LRG sample as in G15 (i-band absolute magnitude $M_i < -21.6$ and $0.48 < z < 0.55$), selected from SDSS-III BOSS CMASS galaxies (Eisenstein et al. 2011; Bolton et al. 2012). Following Guo et al. (2014c), the 3PCF is calculated using the estimator of Szapudi & Szalay (1998). The triangles are represented in the parametrization of (r_1, r_2, θ), with $r_2 \geqslant r_1$ and θ being the angle between $\mathbf{r}_1$ and $\mathbf{r}_2$. We use linear binning schemes for r_1, r_2 and θ, with $\Delta r_1 = \Delta r_2 = 2\,h^{-1}\mathrm{Mpc}$, and $\Delta\theta = 0.1\pi$.

To correct for the fibre collision effect in the redshift-space 3PCF, $\zeta(r_1, r_2, \theta)$, we assign the redshift of each fibre-collided galaxy from its nearest neighbour (Guo et al. 2012, 2014c). To further reduce any residual effect on scales slightly larger than the projected fibre collision scale in SDSS-III ($\sim 0.5\,h^{-1}\mathrm{Mpc}$) (Gunn et al. 2006; Dawson et al. 2013; Smee et al. 2013), we only consider the triangle configurations of $r_2 = 2r_1$ and $r_1 \geqslant 1\,h^{-1}\mathrm{Mpc}$, which will ensure that all sides of the triangle are larger than $1\,h^{-1}\mathrm{Mpc}$. We measure the redshift-space 3PCF for six r_1 bins, centred at $2\,h^{-1}\mathrm{Mpc}$, $4\,h^{-1}\mathrm{Mpc}$, ..., $12\,h^{-1}\mathrm{Mpc}$, with each bin having 10 triangle configurations of different values of θ.

For HOD modelling, we also adopt the 2PCF measurements from G15 and perform a joint fit with the 3PCF, which allows a study of the information content related to the HOD constraints from the 3PCF. The 2PCF measurements include the projected 2PCF (w_p), the monopole (ξ_0), quadrupole (ξ_2) and hexadecapole moments (ξ_4) of the redshift-space 2PCF from 0.13 to $51.5\,h^{-1}\mathrm{Mpc}$ (see G15). The full covariance matrix (including the cross-correlation between the 2PCF and 3PCF measurements) is estimated from $N_{jk} = 403$ jackknife subsamples (G15). To reduce the effect of noise in the covariance matrix, we apply the method of Gaztañaga & Scoccimarro (2005) and only retain the modes that have eigenvalues $\lambda^2 > \sqrt{2/N_{jk}}$. Figure 1 displays the covariance matrix of the 3PCF. In each r_1 bin, the measurements of different θ bins are strongly correlated with each other. The correlation between different r_1 bins is stronger for larger r_1, implying better constraints to the model from the measurements at smaller scales.

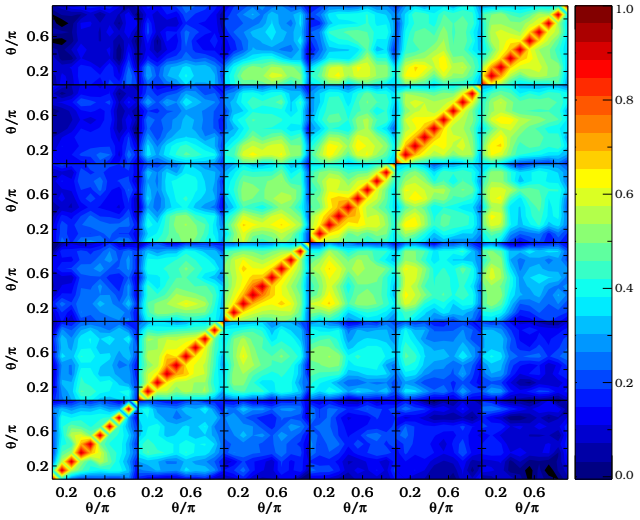

Figure 1. Normalized covariance matrix of the 3PCF. A galaxy triplet is represented by two sides of the triangle, r_1 and $r_2 = 2r_1$, and the angle θ between them. From left to right and bottom to top, the plot shows the normalized covariance matrix for the measurements $\zeta(r_1, r_2, \theta)$ in 10 different θ bins for r_1 centred at 2, 4, 6, 8, 10, and $12\,h^{-1}\mathrm{Mpc}$.

Following G15, we adopt the five-parameter HOD model of Zheng, Coil & Zehavi (2007) and include two additional velocity bias parameters, α_c and α_s, for central and satellite galaxies, respectively. To model the redshift-space 2PCF, we use the simulation-based model of Zheng & Guo (in preparation; see also G15), which is equivalent to populating haloes in the simulations with galaxies for a given HOD prescription. We use the $z = 0.53$ dark matter halo catalogs from the MultiDark simulation (see details in Prada et al. 2012). The haloes are defined using the spherical overdensity (SO) algorithm, with a mean density ∼237 times that of the background universe at $z = 0.53$. The halo centre is defined as the position of the dark matter particle with the minimal potential[1]. We choose the bulk velocity of the inner 25 percent halo particles around the potential minimum as the halo (core) velocity, and the velocity bias is parametrized in this frame, as in G15.

We place the central galaxies at the halo centres, with their ve-

[1] There can be chances that the potential minimum is found in a sub-halo passing close to the halo centre. Even in such a case, assigning the central galaxy to the position of the potential minimum would not affect our modelling result, since the offset from the centre is likely to be smaller than the smallest scales probed by our clustering measurements. In fact, the existence of the central velocity bias itself points to an offset between the central galaxy and halo centre, which is again small compared to the scales we probe (see G15 for more discussions on the expectation and comparison to other observations).

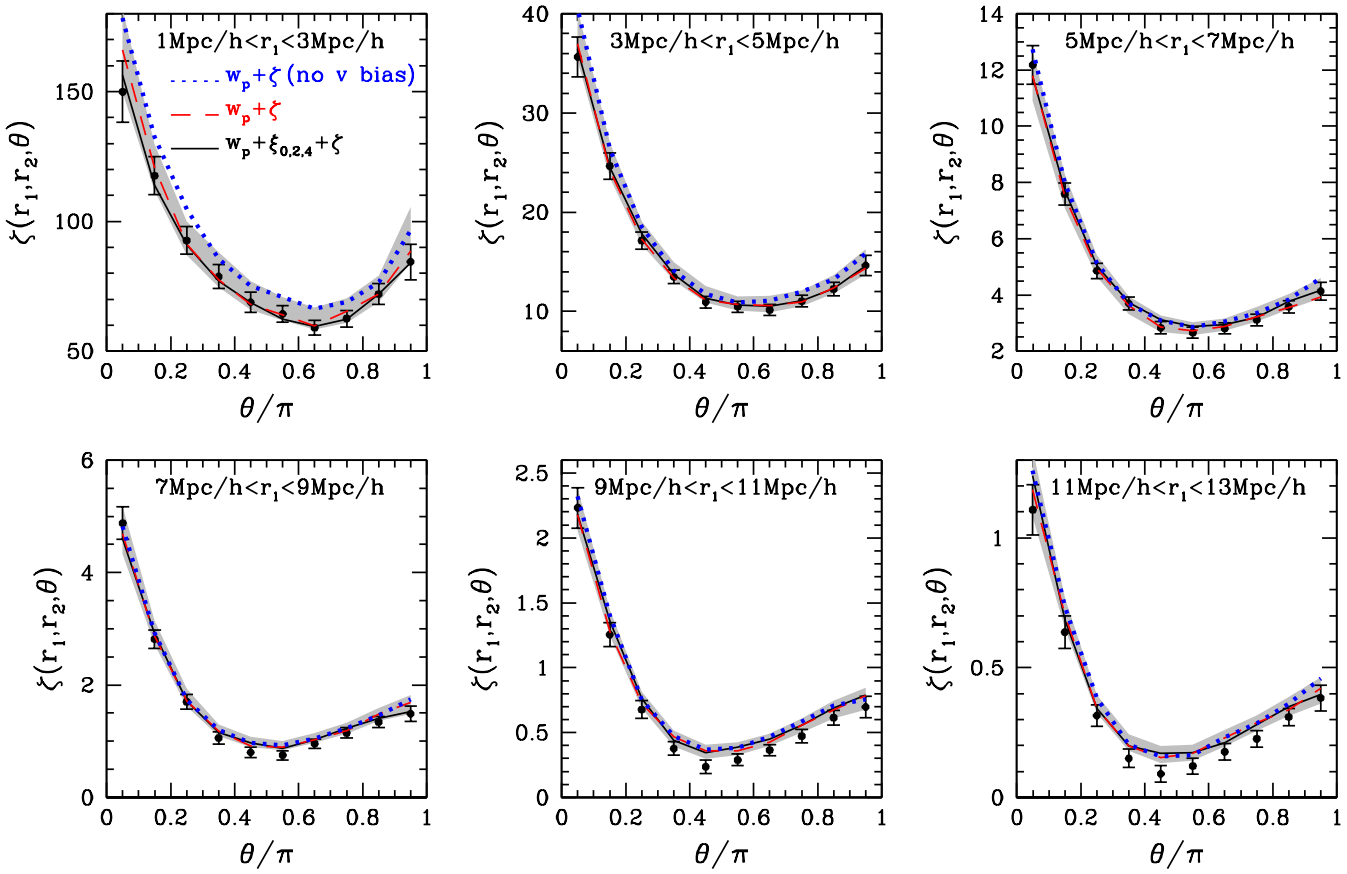

Figure 2. Comparison of the 3PCF measurements (circles with error bars) for BOSS CMASS galaxies to the best-fitting models from HOD fitting to $w_p + \zeta$ (with and without velocity bias) and $w_p + \xi_{0,2,4} + \zeta$. The shaded areas correspond to the 1σ uncertainties in the best-fitting model from fitting $w_p + \xi_{0,2,4} + \zeta$. Different panels display the measurements $\zeta(r_1, r_2, \theta)$ as a function of θ in different r_1 bins ($r_2 = 2r_1$).

locities the same as the halo velocities. For satellite galaxies, we assign the positions and velocities of randomly-selected dark matter particles. We then add the velocity bias effect. The central galaxy velocity bias is parametrized as an additional Gaussian component with zero mean and a standard deviation of $\alpha_c\sigma_v$, where σ_v is the line-of-sight (LOS) velocity dispersion of the dark matter particles in each halo. For the satellite velocity bias, the relative LOS velocity of a satellite galaxy to the halo core is scaled by α_s (as detailed in G15), therefore the 1D satellite galaxy velocity dispersion σ_s is a factor of α_s times that of the dark matter particles, $\sigma_s = \alpha_s\sigma_v$.

To model the 2PCFs and 3PCFs, we apply a Markov chain Monte Carlo method to explore the HOD parameter space. For each set of HOD parameters, the 2PCFs are calculated using the simulation-based model (G15), while the 3PCFs are directly measured from the mock catalogs. The value of χ^2 is the sum of the contribution from the correlation functions and that from the number density of the sample.

3 RESULTS

We explore the constraining power of the 3PCFs on the HOD parameters and the need for including velocity bias parameters by considering three cases. We include w_p in each case, given its common use in constraining the HOD and its effectiveness in limiting the parameter space. First, we perform a joint fit of w_p and the 3PCF ζ with the 5-parameter HOD model without velocity bias (i.e. fixing $\alpha_c = 0$ and $\alpha_s = 1$). This case is denoted as $w_p + \zeta$ (no v bias). Then, we add α_c and α_s as free parameters in the fitting (7 parameters in total), which is denoted as $w_p + \zeta$. The two cases would indicate whether velocity bias is favoured by the data. Finally, we jointly fit all the 2PCF and 3PCF measurements (denoted as $w_p + \xi_{0,2,4} + \zeta$) with the 7-parameter model to obtain the HOD constraints that explain all our measurements.

The best-fitting model predictions of the 3PCFs for the case of $w_p + \zeta$ (no v bias) are shown as dotted blue curves in Figure 2. The best-fitting χ^2 is 59.6, for 70 degrees of freedom (d.o.f.=70, from 14 w_p points, 60 ζ points, one number density point, and 5 parameters). Therefore, the fit without velocity bias is acceptable. Comparing the bestfit to the ζ data points, we notice that on small scales ($r_1 < 5\,h^{-1}\mathrm{Mpc}$) the model overpredicts ζ over all ranges of θ, and on large scales it overpredicts ζ for configurations of nearly degenerate triangles ($\theta \sim 0$ or $\theta \sim \pi$). Even though we cannot judge the fit by eye, given that the data points are correlated, the comparison provides hints to the potential improvements that can be achieved in the modelling. In particular, the small χ^2 could indicate that the covariance matrix is overestimated, and the above differences would signal an inadequacy in the model.

We then introduce the velocity bias parameters α_c and α_s in the modelling. With this 7-parameter model, the best-fitting ζ is shown as the dashed red curve in each panel of Figure 2 (labelled as w_p+ζ). Compared to the case without velocity bias, the fit clearly improves on both small and large scales in a way as expected from the above discussion. The best-fitting χ^2 becomes 46.4 for 68 de-

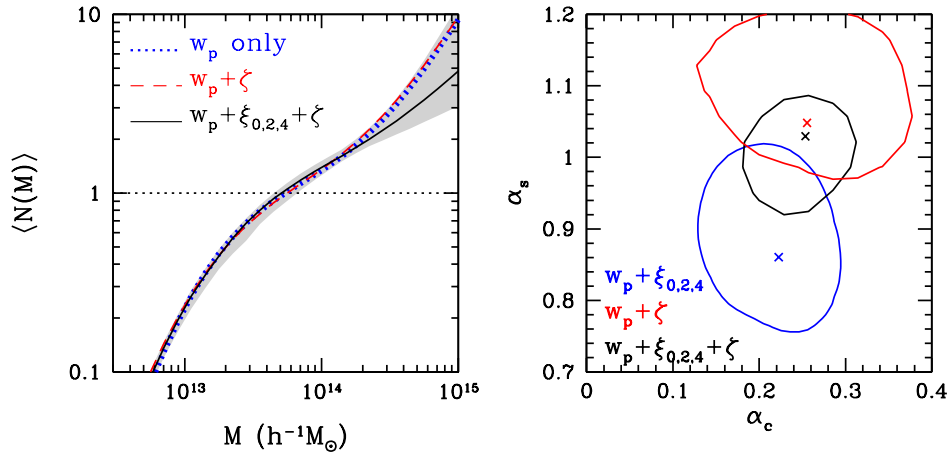

Figure 3. Left: Mean occupation functions of galaxies from different models. The shaded area shows the 1σ distribution around the best-fitting model from jointly fitting w_p, $\xi_{0,2,4}$ and ζ. Right: Constraints to the galaxy velocity bias parameters from fitting various combinations of 2PCFs and 3PCF (see the text). The contours show the 95 per cent confidence levels. The crosses correspond to the parameters from the best-fitting models.

grees of freedom. Putting aside the possibility of overestimation of the covariance matrix, we find that both models with and without velocity bias can fit the data well. Then the question is whether adding the velocity bias is preferred. The Akaike information criterion (AIC; Akaike 1974) provides a quantified way of comparing different models. It penalizes models with more free parameters, $\mathrm{AIC} = \chi^2 + 2\mathrm{N_p}$ with N_p the number of free parameters. To be more conservative, we adopt the AIC with correction (AICc; Konishi & Kitagawa 2007), $\mathrm{AICc} = \mathrm{AIC} + 2\mathrm{N_p}(\mathrm{N_p}+1)/(\mathrm{N_d} - \mathrm{N_p} - 1)$ with N_d the number of data points, which gives more penalty than AIC to the model with more parameters. We find the AICc value to be 70.5 and 62.1 for the models without and with velocity bias, respectively. As a consequence, the model without velocity bias is $\exp((62.1 - 70.5)/2) = 0.015$ times as probable as the model with velocity bias. Therefore, the model with velocity bias is preferred by the data, even though it includes two more free parameters. The possibility that the covariance matrix is overestimated would strengthen this conclusion. The result also implies that the redshift-space 3PCFs can provide constraints on the velocity bias parameters, which is a point we discuss later.

Finally, using the 7-parameter model we perform a joint fit to w_p, $\xi_{0,2,4}$, and ζ. The best-fitting models are shown as the solid black curves in Figure 2, which represents the 3PCF measurements remarkably well on all scales. The overall best-fitting χ^2/dof value, to all measurements, is $97.4/110$. There is a slight over-prediction for triangle configurations of $\theta \sim 0.4\pi$ on scales of $r_1 > 7\,h^{-1}\mathrm{Mpc}$. According to the covariance matrix in Figure 1, the measurements for these triangle configurations are strongly correlated among the neighbouring θ bins, which implies that the fit cannot be simply judged by χ^2-by-eye. The shaded regions are the 1σ uncertainties around this best-fit model. On large scales ($r_1 > 7\,h^{-1}\mathrm{Mpc}$), all three models are consistent within the 1σ uncertainties, with the $w_p+\zeta$ (no v bias) model showing the largest deviation. The three models are more readily separate on smaller scales, where the contribution of the one-halo term (i.e. the contribution from intra-halo galaxy triplets) becomes important. This result indicates that the small-scale 3PCF measurements are important in discriminating the models and in constraining the galaxy distribution within haloes.

Figure 3 shows the constraints on the HOD from different models. In addition to the models in Figure 2, we also include constraints from fitting only 2PCFs statistics (w_p and $\xi_{0,2,4}$). The left panel presents the best-fitting mean occupation functions. The mean occupation functions of central galaxies can already be well constrained by w_p, and the constraints from other models show only small variations. The well-constrained mean occupation function of central galaxies explains why the 3PCFs on large scales are similar for the different models. The best-fitting mean occupation functions from w_p-only or from including ζ are similar. Including all the 2PCFs and 3PCFs lead to a shallower high-mass slope. However, the uncertainty in the high-mass slope is large, as indicated by the shaded region (1σ) for the $w_p + \xi_{0,2,4} + \zeta$ fit, and the satellite mean occupation functions from the different models are in good agreement. In fact, the uncertainty in the high-mass slope is even larger if we do not include the 3PCFs. The 3PCFs thus tighten the constraints on the high-mass slope, as expected from the larger weight towards higher halo mass from the intra-halo galaxy triplets. However, we do not find substantial tightening for the high-mass slope, which results from the lack of 3PCF measurements on scales below $1\,h^{-1}\mathrm{Mpc}$.

The agreement between the mean occupation functions constrained from the w_p-only fit and the joint fit, together with the difference in the corresponding model 3PCFs, suggests that galaxy velocity bias can improve the interpretation of the data. The right panel of Figure 3 shows the velocity bias constraints (contours of 95% confidence level) for the three relevant models.

The velocity bias constraints from $w_p + \xi_{0,2,4}$ (2PCF only statistics) are the same as in G15. When replacing $\xi_{0,2,4}$ with the redshift-space 3PCF ζ, the velocity bias constraints originate from ζ. Indeed, the red contour in the right panel of Figure 3 shows that the 3PCF data favours the existence of central galaxy velocity bias α_c. Note that in this figure, the $w_p + \zeta$ (no v bias) model corresponds to the point at $\alpha_c = 0$ and $\alpha_s = 1$. The value of α_c from fitting $w_p+\zeta$ is consistent with that from the 2PCF constraints. The effect of the central velocity bias can be inferred from the comparison between the $w_p + \zeta$ (no v bias) fit and the $w_p + \zeta$ fit with velocity bias for the 3PCFs on large scales in Figure 2. The model with no velocity bias shows an over-prediction of ζ for nearly degenerate triangle configurations (i.e. $\theta \sim 0$ and $\theta \sim \pi$). Consider the situation in an overdense region, which appears squashed in redshift space along the line of sight because of large-scale infall. The effect of the central velocity bias is to smear out the redshift-space

distribution of galaxies, making the distribution less squashed. A less squashed distribution reduces the possibility of finding degenerate triangle configurations, and thus lowers the amplitude of ζ for $\theta \sim 0$ and $\theta \sim \pi$, leading to a better fit.

In terms of the satellite velocity bias, the 3PCFs prefer to have satellite galaxies moving faster than dark matter ($\alpha_s > 1$). Such a constraint comes mainly from the small-scale ζ, where the Fingers-of-God (FoG) effect in the redshift-space distribution of galaxies contributes. The $\alpha_s > 1$ satellite velocity bias, in combination with the central velocity bias, enhances the FoG. This situation causes the galaxy distribution more extended, and such a dilution reduces the possibility of finding small-scale galaxy triplets, lowering the small-scale 3PCF ζ. This effect clearly explains the difference seen in the small-scale ζ in Figure 2 between the $w_p + \zeta$ fits with and without velocity bias. The satellite velocity bias constraint (red contour) from the 3PCFs shows a tentative tension with that (blue contour) from the 2PCFs, even though it is at a level of $< 2\sigma$. If the tension is confirmed with more accurate measurements, the model would need to be improved, e.g. by introducing freedom in the spatial distribution profiles of satellites inside haloes (see the tests in G15). With the current data, we conclude that combining the measurements of the 2PCFs and the 3PCF significantly strengthens the constraints on the galaxy velocity bias, as demonstrated by the smaller black contour in the right panel of Figure 3.

4 CONCLUSION

In this paper, we measure the redshift-space 3PCFs for a volume-limited sample of LRGs ($0.48 < z < 0.55$) in the SDSS-III BOSS CMASS DR11 data, and perform HOD modelling of the 3PCFs and 2PCFs. Similar to the case with the 2PCFs (G15), the 3PCF measurements favours the existence of galaxy velocity bias, with which we are able to reproduce the observed galaxy 3PCFs remarkably well on all scales larger than $1\,h^{-1}\mathrm{Mpc}$.

By combining with the 2PCFs, the galaxy 3PCFs tighten the constraints on the HOD parameters, because the three-point distribution is more sensitive to the galaxy occupations in more massive haloes (Kulkarni et al. 2007). Both the redshift-space 2PCFs or 3PCFs can be used to constrain galaxy velocity bias. Either of them leads to a consistent central galaxy velocity bias of around 0.25, i.e. on average the central galaxy is in motion with respect to the core of its host halo, corresponding to a 1D velocity dispersion of $\sim 79\,\mathrm{km\,s^{-1}}$ for halo masses around $2 \times 10^{13}\,h^{-1}\mathrm{M}_\odot$ (see G15). The redshift error ($\sim 30\,\mathrm{km\,s^{-1}}$, Bolton et al. 2012; already accounted for in the model) alone is not enough to account for the central velocity bias. As discussed in G15, such a motion is consistent with those inferred from other observations, including the extrapolation from the measurements in galaxy clusters (Lauer et al. 2014). The satellite velocity distribution is consistent with that of the dark matter from either constraint and from the joint one.

As seen from the covariance matrix and the fitting results, the 3PCFs on small scales ($r < 7\,h^{-1}\mathrm{Mpc}$) have stronger constraining power on the HOD parameters (including the velocity bias parameters). Since we limit our measurements of the 3PCF to scales larger than $1\,h^{-1}\mathrm{Mpc}$ to reduce the fibre collision effects, we have only small improvements on constraining the satellite occupation function (compared to those from the 2PCFs) and the constraints to the phase-space distribution of satellite galaxies within haloes are loose. The satellite velocity bias is degenerate with the spatial distribution of satellites within dark matter haloes (see Figure 11 of G15). The 3PCF is more sensitive to the satellite distribution profile, since it probes the profile with triangles of different shapes. The tentative tension of the satellite velocity bias constraints between using $\xi_{0,2,4}$ and ζ (right panel of Figure 3) may indicate the departure of the spatial distribution of satellites from that of the dark matter. Therefore, the small-scale 3PCF measurements may serve as a powerful way of understanding the satellite galaxy distribution within haloes and may provide constraints to the halo assembly bias effect (Zentner, Hearin, & van den Bosch 2014). We plan to explore such a possibility in our future work by using survey samples free of fibre collision effects and by considering small triplet separations.

ACKNOWLEDGMENTS

We thank the anonymous referee for the helpful and constructive comments. ZZ was partially supported by NSF grant AST-1208891. YPJ is supported by 973-project 2015CB857000, NSFC-11320101002, and Shanghai key laboratory grant No. 11DZ2260700. CL acknowledges the support of NSFC (11173045, 11233005, 11325314, 11320101002) and the Strategic Priority Research Program "The Emergence of Cosmological Structures" of CAS (Grant No. XDB09000000). We gratefully acknowledge the use of computing resources at Shanghai Astronomical Observatory, from the High Performance Computing Resource in the Core Facility for Advanced Research Computing at Case Western Reserve University, and from the Center for High Performance Computing at the University of Utah.

Funding for SDSS-III has been provided by the Alfred P. Sloan Foundation, the Participating Institutions, the National Science Foundation, and the U.S. Department of Energy Office of Science. The SDSS-III web site is http://www.sdss3.org/. SDSS-III is managed by the Astrophysical Research Consortium for the Participating Institutions of the SDSS-III Collaboration including the University of Arizona, the Brazilian Participation Group, Brookhaven National Laboratory, University of Cambridge, Carnegie Mellon University, University of Florida, the French Participation Group, the German Participation Group, Harvard University, the Instituto de Astrofisica de Canarias, the Michigan State/Notre Dame/JINA Participation Group, Johns Hopkins University, Lawrence Berkeley National Laboratory, Max Planck Institute for Astrophysics, Max Planck Institute for Extraterrestrial Physics, New Mexico State University, New York University, Ohio State University, Pennsylvania State University, University of Portsmouth, Princeton University, the Spanish Participation Group, University of Tokyo, University of Utah, Vanderbilt University, University of Virginia, University of Washington, and Yale University.

References

Akaike, H. 1974, IEEE Transactions on Automatic Control, 19, 716
Berlind A. A., Weinberg D. H., 2002, ApJ, 575, 587
Bernardeau F., Colombi S., Gaztañaga E., Scoccimarro R., 2002, PhR, 367, 1
Bolton A. S., et al., 2012, AJ, 144, 144
Coil A. L. et al., 2006, ApJ, 644, 671
Dawson K. S., et al., 2013, AJ, 145, 10
Eisenstein D. J., et al., 2011, AJ, 142, 72

Gaztañaga E., Norberg P., Baugh C. M., Croton D. J., 2005, MNRAS, 364, 620
Gaztañaga E., Scoccimarro R., 2005, MNRAS, 361, 824
Gaztanaga E., Frieman J. A., 1994, ApJL, 437, L13
Gunn J. E., et al., 2006, AJ, 131, 2332
Guo H., Jing Y. P., 2009, ApJ, 698, 479
Guo H., Li C., Jing Y. P., Börner G., 2014b, ApJ, 780, 139
Guo H., Zehavi I., Zheng Z., 2012, ApJ, 756, 127
Guo H. et al., 2013, ApJ, 767, 122
Guo H. et al., 2015, MNRAS, 446, 578 (G15)
Guo H. et al., 2014a, MNRAS, 441, 2398
Jing Y. P., Börner G., 2004, ApJ, 607, 140
Jing Y. P., Mo H. J., Boerner G., 1998, ApJ, 494, 1
Konishi, S., & Kitagawa, G. 2007, Information Criteria and Statistical Modelin, Springer Science+Business Media, LLC, New York, NY USA
Kulkarni G. V. et al., 2007, MNRAS, 378, 1196
Lauer T. R., Postman M., Strauss M. A., Graves G. J., Chisari N. E., 2014, ApJ, 797, 82
Li C. et al., 2006, MNRAS, 368, 37
Li C., Jing Y. P., Mao S., Han J., Peng Q., Yang X., Mo H. J., van den Bosch F., 2012, ApJ, 758, 50
Marín F. A., et al., 2013, MNRAS, 432, 2654
McBride C. K. et al., 2011, ApJ, 726, 13
Miyatake H. et al., 2013, ApJ, preprint(arXiv:1311.1480)
Pan J., Szapudi I., 2005, MNRAS, 362, 1363
Peacock J. A., Smith R. E., 2000, MNRAS, 318, 1144
Prada F. et al., 2012, MNRAS, 423, 3018
Reid B. A. et al., 2014, MNRAS, 444, 476
Scoccimarro R. et al., 2001, ApJ, 546, 20
Skibba R. A., Sheth R. K., 2009, MNRAS, 392, 1080
Smee S. A., et al., 2013, AJ, 146, 32
Smith R. E., Sheth R. K., Scoccimarro R., 2008, PhRvD, 78, 023523
Szapudi S., Szalay A. S., 1998, ApJL, 494, L41
Wang Y. et al., 2004, MNRAS, 353, 287
Wang Y. et al., 2007, ApJ, 664, 608
Zehavi I. et al., 2002, ApJ, 571, 172
Zehavi I. et al., 2011, ApJ, 736, 59
Zehavi I. et al., 2005, ApJ, 630, 1
Zentner A. R., Hearin A. P., van den Bosch F. C., 2014, MNRAS, 443, 3044
Zheng Z., 2004, ApJ, 610, 61
Zheng Z. et al., 2005, ApJ, 633, 791
Zheng Z., Coil A. L., Zehavi I., 2007, ApJ, 667, 760
Zheng Z. et al., 2009, ApJ, 707, 554